

NEUROSCIENCE

Hippocampal ripples down-regulate synapses

Hiroaki Norimoto,^{1,2} Kenichi Makino,^{1,*} Mengxuan Gao,^{1,*} Yu Shikano,¹ Kazuki Okamoto,¹ Tomoe Ishikawa,¹ Takuya Sasaki,¹ Hiroyuki Hioki,^{3,4} Shigeyoshi Fujisawa,^{2,†} Yuji Ikegaya^{1,5,†}

The specific effects of sleep on synaptic plasticity remain unclear. We report that mouse hippocampal sharp-wave ripple oscillations serve as intrinsic events that trigger long-lasting synaptic depression. Silencing of sharp-wave ripples during slow-wave states prevented the spontaneous down-regulation of net synaptic weights and impaired the learning of new memories. The synaptic down-regulation was dependent on the *N*-methyl-D-aspartate receptor and selective for a specific input pathway. Thus, our findings are consistent with the role of slow-wave states in refining memory engrams by reducing recent memory-irrelevant neuronal activity and suggest a previously unrecognized function for sharp-wave ripples.

Hippocampal and neocortical plasticity during the awake state is dominated by net synaptic potentiation, whereas plasticity during sleep, especially during slow-wave (SW) sleep, is dominated by net synaptic depression (1, 2). These circadian alternations in synaptic weights manifest a homeostatic balancing function for sleep (3, 4); however, the mechanisms behind the synaptic downscaling during SW states remain to be identified. During SW states—which include SW sleep, awake immobility, and consummatory behavior—the hippocampus spontaneously emits transient high-frequency field oscillations called sharp-wave ripples (SWRs) (fig. S1). SWRs represent the reactivation of neurons involved in recently acquired memory (5) and contribute to memory consolidation (6–9). Although memory consolidation may rely on synaptic plasticity, no consensus has yet been reached on the relationship between SWRs and synaptic plasticity (10–12).

We first investigated whether suppression of SWRs affects the synaptic down-regulation that occurs during SW states. We allowed mice to explore novel environments for 30 min before sleep because SWRs are known to occur more frequently after spatial learning (13). Indeed, the 30-min exploration increased the SWR event frequencies from 0.48 ± 0.03 Hz under naïve conditions to 0.88 ± 0.07 Hz (mean \pm SEM of eight trials from three mice; $P = 3.1 \times 10^{-8}$, $t_7 = 6.56$, paired *t* test). The SWR increase may reflect the strengthening of synaptic weights in the learning process (14). We then perturbed the SWRs

during SW states for 7 hours by using optogenetic feedback stimulation triggered upon the online detection of ripples in local field potentials (LFPs) recorded from the hippocampal CA1 region (Fig. 1A) (15). Simultaneous LFP recordings and electromyograms revealed that $84.6 \pm 2.9\%$ of the SW periods over 7 hours coincided with SW sleep, whereas the remaining SW periods were detected during awake immobility or consummatory behavior. Feedback illumination but not time-mismatched control illumination with random delays ranging from 80 to 120 ms to the dorsal CA3 region of somatostatin (SOM)::channelrhodopsin2 (ChR2) transgenic mice (Fig. 1B) reduced both ripple power (Fig. 1C) and the firing rates of CA1 pyramidal cells during the SWRs (Fig. 1C). This closed-loop technique silenced $97.7 \pm 1.8\%$ of the total SWRs (mean \pm SEM of 10 trials from five mice). We measured field excitatory postsynaptic potentials (fEPSPs) from the CA1 stratum radiatum while single-pulse field stimulation was applied every 20 s to the Schaffer collaterals, which per se did not induce SWRs. Consistent with previous studies (1), the fEPSP slopes in no-light control and delayed control groups gradually decreased during the SW periods, but this spontaneous synaptic depression did not occur in the SWR-silenced mice (Fig. 1D). Neither the total sleep length nor the percentage occupied by each brain state differed between the groups (fig. S2), but the event incidence of SWRs remained higher in the SWR-silenced group (fig. S3).

After the SWRs were silenced for 7 hours, animals were tested in an object-place recognition task that consisted of two phases (Fig. 1E). During the first encoding phase, mice explored a familiar open arena with two identical novel objects, and none of the mouse groups exhibited a preference for one object over the other (fig. S4). The second recall phase, in which one of the objects was moved to a previously empty location, was conducted after a 2-hour resting period in the home cages. In this phase, the SWR-silenced group did not discriminate between the relocated and unmoved objects (Fig. 1F). Thus, object-place learning was disturbed after SWR silencing during SW states.

To more directly examine whether SWRs induce synaptic depression, we used obliquely sliced hippocampal preparations (16), which spontaneously emit SWRs (fig. S5). Slices prepared from animals that had explored a novel environment for 30 min exhibited higher SWR event frequencies than slices from naïve mice (fig. S5). Therefore, in the following experiments, we used slices from animals after exploration. Single-pulse field stimulation was applied to the Schaffer collaterals, and fEPSPs were recorded from the CA1 stratum radiatum. The fEPSP slopes were spontaneously reduced over time, and this reduction was inhibited by bath application of $50 \mu\text{M}$ D-AP5, an *N*-methyl-D-aspartate receptor (NMDAR) antagonist (fig. S6A). Thus, the spontaneous depression reflected actively occurring synaptic plasticity (17) rather than deterioration of the slice preparations or synaptic fatigue. We also prepared conventional horizontal hippocampal slices, which do not emit SWRs (16). Although these slices did not exhibit spontaneous synaptic depression (fig. S6B), even without SWRs, synaptic depression was inducible in a D-AP5-sensitive manner when the Schaffer collaterals were repetitively stimulated at event timings of the SWRs recorded in vivo after spatial exploration but not under naïve conditions without exploration (fig. S7).

We used slices prepared from SOM::ChR2 mice to conduct closed-loop SWR inhibition (Fig. 2A). Blue light pulsed upon SWR detection suppressed the firing rates of the neurons during SWRs (Fig. 2B). The SWR silencing prevented spontaneous synaptic depression, whereas control stimulation with a delay of 100 ms failed to replicate this effect (Fig. 2C).

We next attempted to confirm the spontaneous synaptic depression in SWR-emitting slices at the single-synapse level. The head sizes of dendritic spines are correlated with synaptic strength (18, 19) and are subject to shrinkage during NMDAR-dependent long-term depression (20). We therefore examined whether spine shrinkage accompanied the spontaneous synaptic depression. We prepared oblique hippocampal slices from Thy1-mGFP mice and performed two-photon imaging of spines on the apical dendrites of CA1 pyramidal cells for 180 min (fig. S8A). The mean head volume of the spines decreased spontaneously as a function of time, an effect that was blocked by $50 \mu\text{M}$ D-AP5 (fig. S8B). The mean density of the spines did not change, indicating that few spines disappeared during the recording time ($P = 0.686$, $U = 6.00$, Mann-Whitney *U* rank sum test). As spines are typically categorized into thin, stubby, and mushroom types, we separately analyzed spine shrinkage for these types (fig. S8C, left). Thin and stubby spines shrank in a D-AP5-sensitive manner, but mushroom spines maintained their volumes throughout our observation period (fig. S8C, right).

Given the heterogeneity and specificity in spine shrinkage, we reasoned that patterns of CA1 neuronal activity may also be modulated in an NMDAR-dependent manner, because individual synaptic weights collectively orchestrate patterns of neuronal activity (21). Arc-dVenus transgenic mice (22) were allowed to freely explore a

¹Laboratory of Chemical Pharmacology, Graduate School of Pharmaceutical Sciences, The University of Tokyo, Tokyo, Japan. ²Laboratory for Systems Neurophysiology, RIKEN Brain Science Institute, 2-1 Hirosawa, Wako City, Saitama, Japan. ³Department of Morphological Brain Science, Graduate School of Medicine, Kyoto University, Kyoto, Japan. ⁴Department of Cell Biology and Neuroscience, Juntendo University Graduate School of Medicine, Tokyo, Japan. ⁵Center for Information and Neural Networks, National Institute of Information and Communications Technology, Osaka, Japan.

*These authors contributed equally to this work.

†Corresponding author. Email: yuji@ikegaya.jp (Y.I.); fujisawa@brain.riken.jp (S.F.)

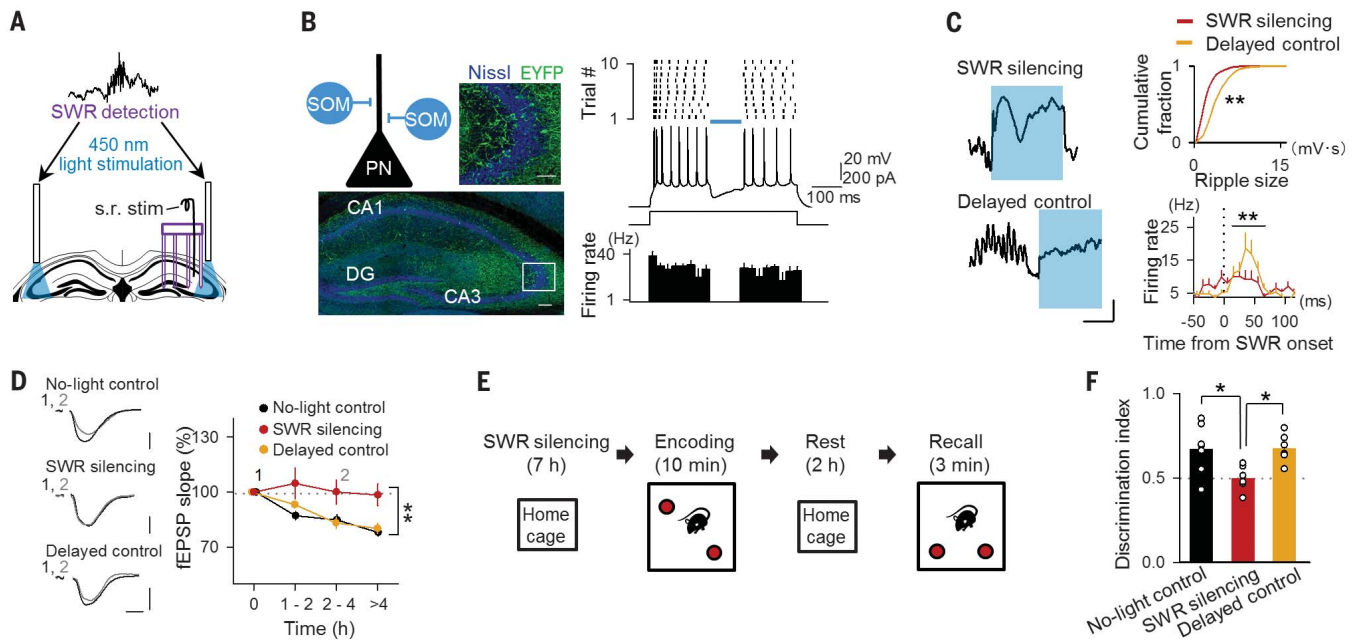


Fig. 1. SWR silencing prevents spontaneous synaptic depression during SW states and impairs subsequent spatial memory acquisition.

(A) Schematic illustration of closed-loop SWR silencing. CA1 ripples were detected in real time after the experimental onset, triggering blue-light illumination targeting the bilateral dorsal CA3 region. s.r. stim., stratum radiatum stimulation. (B) (Left) Representative confocal image showing SOM::Chr2-enhanced yellow fluorescent protein (EYFP) expression in a hippocampal section that was counterstained with fluorescent Nissl. The boxed region is magnified in the top right image. Scale bars, 100 μm (top right) and 50 μm (bottom). DG, dentate gyrus. The top left image illustrates inhibition of a pyramidal neuron (PN) by SOM-positive interneurons. (Right) Whole-cell patch clamp recording showing that blue-light illumination suppressed current injection-evoked spiking in pyramidal cells. $n = 5$ cells in five slices from three mice. (C) (Left) Examples of the online feedback illumination (top) and control illumination with a delay (bottom). Scale bars, 0.2 mV (vertical) and 50 ms (horizontal). (Right) SWR silencing via SOM activation suppressed the ripple size (top) and SWR-locked units (bottom) recorded from CA1 shanks. Delayed illumination was used as a control. Kolmogorov-Smirnov test: $**P = 2.7 \times 10^{-154}$.

$D_{3693} = 0.437$, $n = 1731$ (silencing) and 1962 (delayed) ripples from six mice each. Mann-Whitney U rank sum test: $P = 1.0 \times 10^{-3}$, $U = 34770$, $n = 18$ (silencing) and 21 (delayed) cells from six mice. (D) Time course of the fEPSP slopes normalized at 0 min. SWR silencing during SW states suppressed the spontaneous fEPSP attenuation that occurred in the control groups. The images at left show typical fEPSP traces at times 1 and 2. Scale bars, 2 mV (vertical) and 5 ms (horizontal). Two-way analysis of variance (ANOVA), $n = 6$ mice each: $**P = 5.5 \times 10^{-4}$, $F_{1,28} = 15.19$ versus no-light control; $**P = 1.2 \times 10^{-3}$, $F_{1,30} = 12.90$ versus delayed control. (E) Behavioral paradigm. After SWR silencing in a home cage for 7 hours, mice were exposed to two identical objects for 10 min (encoding phase). After a 2-hour rest in the home cage, the mice were allowed to explore the same arena for 3 min with one of the objects relocated to the opposite corner (recall phase). The preferential exploration of the relocated object was measured as memory recall. (F) Discrimination indices during the recall phase were computed during the first 3 min of exploration. The SWR-silenced mice did not discriminate between the objects. Tukey's test after one-way ANOVA, $n = 6$ or 7 mice: $*P = 0.031$, $Q_{3,16} = 4.00$ versus no-light control; $*P = 0.033$, $Q_{3,16} = 3.96$ versus delayed control.

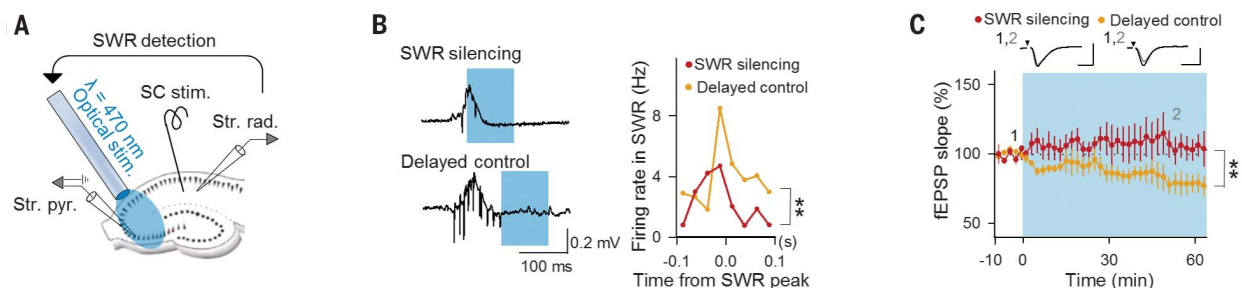


Fig. 2. Inhibiting hippocampal neurons during SWR impairs spontaneous synaptic depression in SWR-emitting slices.

(A) Experimental procedures for recording fEPSPs at CA3 and CA1 synapses and silencing SWRs. SWRs and fEPSPs in the CA1 region were monitored in hippocampal slices prepared from SOM::Chr2-EYFP transgenic mice. A stimulating electrode was placed on the CA1 stratum radiatum to stimulate Schaffer collateral (SC) afferents. As SWRs were detected online, blue-light pulses were applied through an objective lens located over the CA3 region. Str. rad., stratum radiatum; Str. pyr., stratum pyramidale. (B) (Left) Examples of online feedback illumination (top) and delayed control illumination with a delay of 100 ms (bottom). Cyan boxes indicate the periods of light illumination. (Right) SOM activation during SWRs, but not outside of SWRs, suppressed SWR-locked multiunits. Z test for comparing two counts, $n = 3197$ and 863 events: $**P = 4.0 \times 10^{-13}$. (C) Time course of the fEPSP slopes after closed-loop illumination. SWR silencing but not delayed control impaired the spontaneous fEPSP depression. The slopes were normalized to the 10-min baseline values. The insets show typical fEPSP traces at times 1 and 2. Scale bars, 0.3 mV (vertical) and 20 ms (horizontal). Two-way ANOVA, $n = 5$ slices: $**P = 3.1 \times 10^{-15}$, $F_{1,237} = 71.3$.

control illumination with a delay of 100 ms (bottom). Cyan boxes indicate the periods of light illumination. (Right) SOM activation during SWRs, but not outside of SWRs, suppressed SWR-locked multiunits. Z test for comparing two counts, $n = 3197$ and 863 events: $**P = 4.0 \times 10^{-13}$. (C) Time course of the fEPSP slopes after closed-loop illumination. SWR silencing but not delayed control impaired the spontaneous fEPSP depression. The slopes were normalized to the 10-min baseline values. The insets show typical fEPSP traces at times 1 and 2. Scale bars, 0.3 mV (vertical) and 20 ms (horizontal). Two-way ANOVA, $n = 5$ slices: $**P = 3.1 \times 10^{-15}$, $F_{1,237} = 71.3$.

novel environment for 30 min (Fig. 3A) and were euthanized for hippocampal slice preparations. Cells positive for the modified yellow fluorescent protein dVenus (dVenus⁺) putatively corresponded to neurons that had been activated during the exploration of the novel environment (16). We monitored the activity of CA1 neurons by functional calcium imaging while recording CA1 LFPs

(Fig. 3B). Although dVenus⁺ and dVenus⁻ neurons were both activated during SWRs, dVenus⁺ neurons tended to be more likely to participate in SWRs than dVenus⁻ neurons (Fig. 3C). After 40 min, this difference increased further; that is, the SWR participation probability (the mean probability that a given cell exhibited a calcium transient during a given SWR event) became

significantly higher for dVenus⁺ cells than for dVenus⁻ cells, mainly through a decrease in the participation probability in dVenus⁻ cells (Fig. 3D). The participation probability of neither dVenus⁺ nor dVenus⁻ cells was altered by treatment of slices with D-AP5 (Fig. 3E). Thus, the proportion of dVenus⁺ cells in the cells activated during SWRs increased over time.

Fig. 3. NMDAR regulates the refinement of in vitro engram reactivation. (A) Experimental procedures for the in vitro SWR assay using hippocampal slices prepared from Arc-dVenus mice that had explored a novel environment for 30 min. (B) (Top) Calcium imaging from dVenus⁺ and dVenus⁻ CA1 neurons loaded with Fura-2AM. (Bottom) Three representative traces of the Fura-2AM-loaded neurons. *F*, fluorescence. (C) Representative raster plot of 39 simultaneously recorded CA1 cells around 0 and 40 min. The first set of images was taken 5 min after the SWR event frequency reached 0.80 Hz (see materials and methods for details). (D) The participation probability of dVenus⁻ neurons during SWRs (participation rates) was smaller at 40 min than at 0 min, whereas the participation probability of dVenus⁺ neurons did not change over time. dVenus⁻ at 0 min versus dVenus⁻ at 40 min: $**P = 8.0 \times 10^{-5}$, $U = 15,991$; dVenus⁺ at 40 min versus dVenus⁻ at 40 min: $**P = 3.2 \times 10^{-5}$, $U = 1960$; Mann-Whitney U rank sum test with Bonferroni's correction. Error bars indicate SEM of 192 dVenus⁻ and 31 dVenus⁺ cells. (E) The participation probability of neither dVenus⁺ nor dVenus⁻ neurons in slices treated with 50 μ M D-AP5 differed between 0 and 40 min. dVenus⁺: $P = 0.47$, $U = 488.5$; dVenus⁻: $P = 0.34$, $U = 10,571$. Error bars indicate SEM of 39 dVenus⁻ and 145 dVenus⁺ cells.

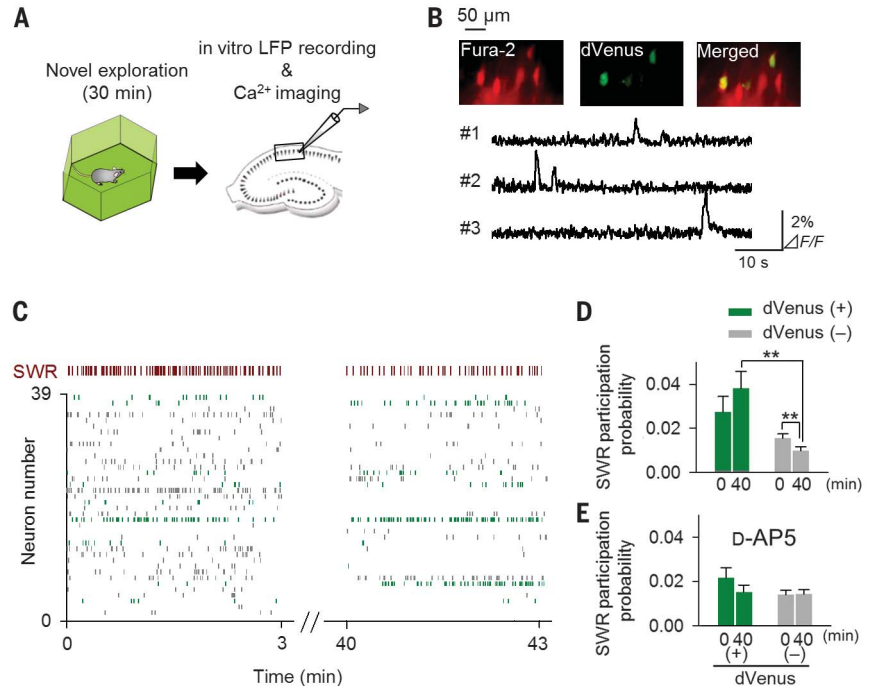
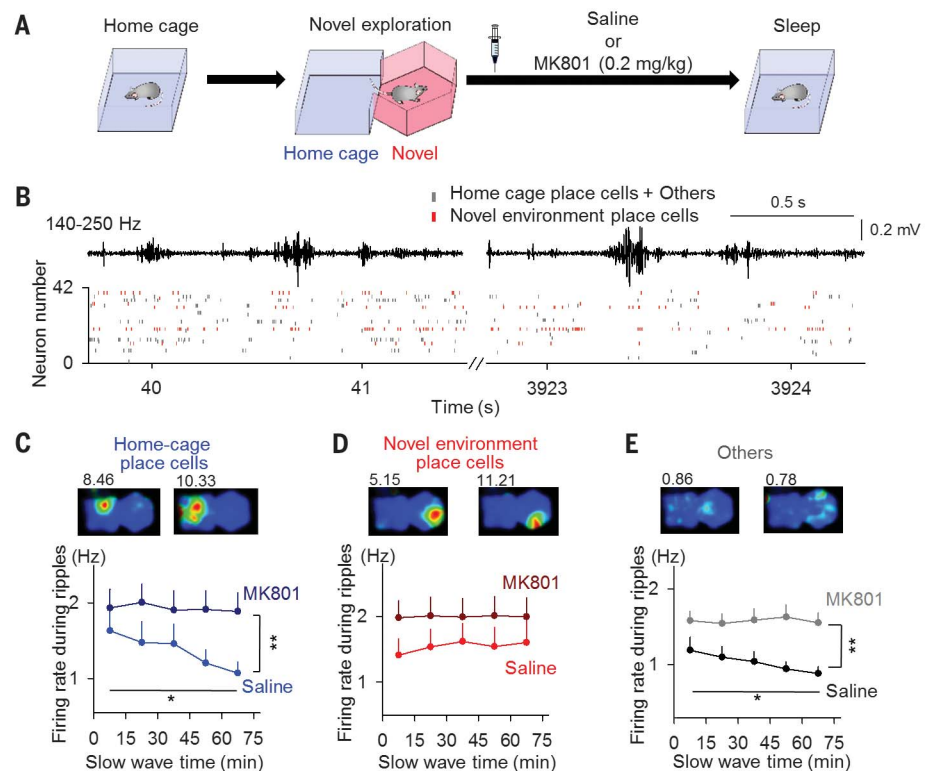


Fig. 4. NMDAR regulates the refinement of memory reactivation. (A) Time course of the experimental procedures. (B) Examples of representative spike events in a sleep session. The red rectangles indicate spikes of neurons that had place fields in the novel environment. The top traces represent ripple-band LFPs. (C to E) (Top) Color-coded rate maps for neurons with place fields in the home cage (C) and novel environment (D) and for other nonplace cells (E). The numbers above the maps represent the peak firing rates (hertz). (Bottom) Time courses of firing rates in SWRs during SW periods. SWR-relevant firing rates of home-cage place cells and other cells, but not novel-environment place cells, decreased with time, an effect that was abolished by the systemic injection of MK801. Home-cage place cells: $*P = 0.048$, $Z = -5.88$; others: $*P = 0.026$, $Z = -1.95$; Jonckheere-Terpstra trend test. Home-cage place cells: $P = 7.3 \times 10^{-4}$, $F_{1,368} = 11.6$; others: $P = 8.5 \times 10^{-4}$, $F_{1,1470} = 11.1$; two-way ANOVA. $n = 37$ to 145 cells from eight or nine trials from three mice (saline) and 28 to 195 cells from eight or nine trials from three mice (MK801).



Finally, we examined whether an NMDAR-dependent refinement of neuronal activity during SWRs also occurs in vivo. Mice were implanted with 32-site silicon probes in the CA1 region to monitor LFPs and unit spikes while the mice traversed their home cages. Each home cage was immediately joined to a novel environment that was not accessible to the mice unless an experiment was being conducted. During the 30-min exploration period in the novel environment, new place cells were detected in addition to the pre-established place cells in the home cage. Immediately after the exploration, the mice were treated intraperitoneally with either saline or 0.2 mg of MK801, an NMDAR blocker, per kilogram of body weight (Fig. 4A). Then, the mice were placed in the original home cage for 4 to 6 hours, and spikes during SW states were analyzed. The place cells were reactivated during SWRs (Fig. 4B). In the saline group, the novel-environment place cells did not change their firing rates during the SWRs throughout the entire recording session, whereas the home-cage place cells and the other cells that did not code either place in the environment (others) gradually decreased their SWR-related firing rates (Fig. 4, C to E). In the MK801-treated group, neither neuron type exhibited such delays in the firing rates (Fig. 4, C to E).

We discovered that hippocampal SWRs triggered persistent synaptic depression and that silencing SWRs impaired subsequent new learning, which appears to be consistent with the hypothesis that overstrengthened synapses impair neuronal responsiveness and saturate the ability to learn (23, 24). We consider three possible but not mutually exclusive mechanisms by which SWRs induce synaptic depression: (i) synaptic delay lines in activity propagation during SWRs decouple hippocampal network activity and weaken synaptic weights (10), (ii) uncorrelated presynaptic and postsynaptic activity during SWRs causes heterosynaptic depression because memory-irrelevant cells are rarely fired during SWRs (25), and (iii) the event frequency of SWRs reaches ~1 Hz after spatial exploration, which may induce homosynaptic depression (26, 27). Notably, field

stimulation with the event timing of SWRs after spatial exploration was sufficient to induce depression, suggesting the importance of the role of the timing, rather than the spike contents, of SWRs. On the other hand, mushroom spines did not shrink in SWR-emitting slices; that is, not all spines were equally subject to depression. This finding is in agreement with the hypothesis that sleep leads to net depression through the removal of unstable synapses [(28), but see also (29)]. A recent in vitro study demonstrated that the relative spike timings of CA3 and CA1 place cells during SWRs cause synaptic potentiation (9). Thus, synapses involved in memory engrams may escape depression through presynaptic and postsynaptic coactivation. Together with our findings, we propose dual roles of SWR-induced depression: (i) SWRs reset unnecessary synapses and avoid memory saturation (30), and (ii) SWRs purify recent memory engrams by shearing irrelevant neuronal activity and perhaps strengthening memory-relevant synapses, thereby contributing to memory consolidation.

REFERENCES AND NOTES

1. V. V. Vyazovskiy, C. Cirelli, M. Pfister-Genskow, U. Faraguna, G. Tononi, *Nat. Neurosci.* **11**, 200–208 (2008).
2. R. Huber *et al.*, *Cereb. Cortex* **23**, 332–338 (2013).
3. G. Tononi, C. Cirelli, *Brain Res. Bull.* **62**, 143–150 (2003).
4. G. Tononi, C. Cirelli, *Neuron* **81**, 12–34 (2014).
5. A. K. Lee, M. A. Wilson, *Neuron* **36**, 1183–1194 (2002).
6. V. Ego-Stengel, M. A. Wilson, *Hippocampus* **20**, 1–10 (2010).
7. G. Girardeau, K. Benchenane, S. I. Wiener, G. Buzsáki, M. B. Zugaro, *Nat. Neurosci.* **12**, 1222–1223 (2009).
8. G. M. van de Ven, S. Trouche, C. G. McNamara, K. Allen, D. Dupret, *Neuron* **92**, 968–974 (2016).
9. J. H. Sadowski, M. W. Jones, J. R. Mellor, *Cell Rep.* **14**, 1916–1929 (2016).
10. E. V. Lubenov, A. G. Siapas, *Neuron* **58**, 118–131 (2008).
11. L. L. Colgin, D. Kubota, Y. Jia, C. S. Rex, G. Lynch, *J. Physiol.* **558**, 953–961 (2004).
12. O. Bukalo, E. Campanac, D. A. Hoffman, R. D. Fields, *Proc. Natl. Acad. Sci. U.S.A.* **110**, 5175–5180 (2013).
13. O. Eschenko, W. Ramadan, M. Mölle, J. Born, S. J. Sara, *Learn. Mem.* **15**, 222–228 (2008).
14. C. J. Behrens, L. P. van den Boom, L. de Hoz, A. Friedman, U. Heinemann, *Nat. Neurosci.* **8**, 1560–1567 (2005).
15. E. Stark *et al.*, *Neuron* **83**, 467–480 (2014).
16. M. Mizunuma *et al.*, *Nat. Neurosci.* **17**, 503–505 (2014).
17. G. L. Collingridge, S. J. Kehil, H. McLennan, *J. Physiol.* **334**, 33–46 (1983).
18. M. Matsuzaki *et al.*, *Nat. Neurosci.* **4**, 1086–1092 (2001).
19. M. Masugi-Tokita *et al.*, *J. Neurosci.* **27**, 2135–2144 (2007).
20. Q. Zhou, K. J. Homma, M. M. Poo, *Neuron* **44**, 749–757 (2004).
21. O. Paulsen, T. J. Sejnowski, *Curr. Opin. Neurobiol.* **10**, 172–179 (2000).
22. M. Eguchi, S. Yamaguchi, *Neuroimage* **44**, 1274–1283 (2009).
23. D. Balduzzi, G. Tononi, *Theory Biosci.* **132**, 27–39 (2013).
24. S. S. Yoo *et al.*, *Nat. Neurosci.* **10**, 385–392 (2007).
25. G. S. Lynch, T. Dunwiddie, V. Gribkoff, *Nature* **266**, 737–739 (1977).
26. R. M. Mulkey, R. C. Malenka, *Neuron* **9**, 967–975 (1992).
27. S. M. Dudek, M. F. Bear, *Proc. Natl. Acad. Sci. U.S.A.* **89**, 4363–4367 (1992).
28. L. de Vivo *et al.*, *Science* **355**, 507–510 (2017).
29. G. H. Diering *et al.*, *Science* **355**, 511–515 (2017).
30. M. R. Mehta, *Nat. Neurosci.* **10**, 13–15 (2007).

ACKNOWLEDGMENTS

We thank C. Cirelli, L. Fenk, Y. Goda, G. Laurent, T. McHugh, S. Reiter, and G. Tononi for comments on early versions of the manuscript; T. Danjo and Y. K. Park for technical assistance; and S. Yamaguchi for providing Arc-dVenus mice. **Funding:** This work was supported by Ministry of Education, Culture, Sports, Science and Technology Grants-in-Aid for Scientific Research (25119004 and 26250003 to Y.I. and 16H01519 to S.F.); “Resonance Bio” (16H01426 to H.H.); Japan Society for the Promotion of Science Grant-in-Aid for Research Activity start-up (16H07453 to H.N.); RIKEN Special Postdoctoral Researchers Program research grant (201600059347 to H.N.); the Sasakawa Scientific Research Grant from the Japan Science Society (28-402 to H.N.); Brain/MINDS (Brain Mapping by Integrated Neurotechnologies for Disease Studies) from the Japan Agency for Medical Research and Development (AMED) (to H.H. and S.F.); the Strategic Research Program for Brain Sciences on “Development of BMI Technologies for Clinical Application” (to Y.I.); and a Human Frontier Science Program (RGP0019/2016 to Y.I.). This work was partly facilitated by a program in the International Research Center for Neurointelligence (WPI-IRCN) of The University of Tokyo Institutes for Advanced Study at The University of Tokyo. **Author contributions:** H.N., S.F., and Y.I. designed and implemented the study and wrote the manuscript. H.N., Y.S., and S.F. performed in vivo physiology. K.M. performed immunohistochemistry. H.N., M.G., and K.O. performed in vitro electrophysiology. H.N. and T.I. performed optical recording. T.S. and H.H. helped with analysis. All authors discussed the results and commented on the manuscript. **Competing interests:** The authors declare no competing interests. **Data and materials availability:** All data necessary to support this paper’s conclusions are available in the main paper or the supplementary materials. The full primary data are available at http://ikegaya.jp/data/norimoto_science2018/.

SUPPLEMENTARY MATERIALS

www.sciencemag.org/content/359/6383/1524/suppl/DC1
Materials and Methods
Figs. S1 to S8
References (31–42)

10 June 2017; accepted 26 January 2018
Published online 8 February 2018
10.1126/science.aao0702



Supplementary Materials for

Hippocampal ripples down-regulate synapses

Hiroaki Norimoto, Kenichi Makino,* Mengxuan Gao,* Yu Shikano, Kazuki Okamoto, Tomoe Ishikawa, Takuya Sasaki, Hiroyuki Hioki, Shigeyoshi Fujisawa,† Yuji Ikegaya†

*These authors contributed equally to this work.

†Corresponding author. Email: yuji@ikegaya.jp (Y.I.); fujisawa@brain.riken.jp (S.F.)

Published 8 February 2018 on *Science* First Release
DOI: 10.1126/science.aao0702

This PDF file includes:

Materials and Methods
Figs. S1 to S8
References

Correction: A citation (reference 30 by M. R. Mehta) was mistakenly omitted from the previous version. This error has been corrected.

Materials and Methods:

Animals

The animal experiments were performed with the approval of the animal experiment ethics committee at the University of Tokyo (approval number: 24-10) and RIKEN (approval number: 2015-049, H28-2-215) according to the University of Tokyo and RIKEN guidelines for the care and use of laboratory animals and in accordance with the Fundamental Guidelines for Proper Conduct of Animal Experiment and Related Activities in Academic Research Institutions (Ministry of Education, Culture, Sports, Science and Technology, Notice No. 71 of 2006), the Standards for Breeding and Housing of and Pain Alleviation for Experimental Animals (Ministry of the Environment, Notice No. 88 of 2006), and the Guidelines on the Method of Animal Disposal (Prime Minister's Office, Notice No. 40 of 1995). The mice were housed 2–4 per cage and kept at $22 \pm 1^\circ\text{C}$ with *ad libitum* access to food and water on a 12-h light/dark cycle (lights on from 7 a.m. to 7 p.m. (the University of Tokyo) and from 8 a.m. to 8 p.m. (RIKEN)). Adult male C57BL/6J mice, weighing 24–34 g and aged 8–13 weeks, were used for the behavioral experiments. Male C57BL/6J mice and somatostatin (SOM)::channelrhodopsin-2 (ChR2) mice, aged 8–14 weeks, were used for the *in vivo* electrophysiology experiments. Juvenile male or female C57BL/6J mice, SOM-ChR2, Thy1-mGFP mice (31), and Arc-dVenus mice (22), aged 3 weeks, were used for *in vitro* electrophysiology. Juvenile male or female Arc-dVenus transgenic mice, aged 3 weeks, were used for functional calcium imaging of behaviorally activated neurons.

Drugs

MK801 was applied intraperitoneally at a dose of 0.2 mg/kg. D-2-Amino-5-phosphonopentanoic acid (D-AP5) was dissolved at 10 mM in water and stored at 4°C . Immediately before use, D-AP5 was diluted to its final concentrations with artificial cerebrospinal fluid (aCSF) containing (in mM) 127 NaCl, 3.5 KCl, 1.24 KH_2PO_4 , 1.2 MgSO_4 , 2.0 CaCl_2 , 26 NaHCO_3 , and 10 D-glucose.

Object-place recognition task

Before the behavioral task, a 6-day successive handling procedure and 2-day successive 10-min habituation were performed in the behavioral arena, which was a $30 \times 30 \times 30\text{-cm}^3$ open cubic arena with transparent walls and a smooth brown floor. Objects were used as visual cues. During the encoding periods, two identical objects were placed in the corner of the arena with the visual cue. During the recall periods, one of the objects was displaced to the corner diagonal from the other object. The mice were allowed to explore the arena for 10 min during the encoding periods and for 3 min during the recall periods. The encoding and recall periods were separated by a home-cage resting period of 2 h and began at 7:30–8:30 and 9:30–10:30 PM, respectively. A discrimination ratio was calculated for each mouse as $T2/(T1+T2)$, where T1 and T2 represent the time spent exploring the familiar object and the displaced object, respectively. The arena and objects were cleaned with 70% ethanol before each experiment. Exploration was defined as sniffing or touching the object with the nose or forepaws. Sitting on the object was not considered exploration. All trials were recorded using a top-view camera, and the exploration time was measured by an experimenter blinded to the behavioral conditions.

All animals were allowed to explore the novel environment for 30 min before the closed-loop stimulation session began.

Animal preparations and *in vivo* electrophysiology

Three C57BL/6J mice and twelve SOM::ChR2-EYFP mice were implanted with silicon probes for chronic recordings of neuronal activity. The general surgical procedures for chronic recordings were described in our previous paper (32). We used Buzsaki32 or A4×8 multichannel probes that consisted of 4 shanks (200 μm/400 μm shank separation); each shank had 8 recording sites that were staggered to provide a two-dimensional arrangement at a vertical separation of 20 μm/100 μm. The mice were implanted with a silicon probe in the CA1 area (AP = -1.9 mm, ML = 1.7 mm; the shanks were aligned parallel to the septotemporal axis of the hippocampus, *i.e.*, 45° parasagittal). The silicon probe was attached to a micromanipulator and was moved gradually to the desired depth position. After the initial surgery, every animal was singly housed. During the recording sessions, the wide-band neurophysiological signals were acquired continuously at 20 kHz. The wide-band signal was down-sampled to 1.25 kHz and was used as the local field potential (LFP) signal. Spike sorting was performed (33), followed by manual adjustment of the clusters. Each unit was classified as a putative pyramidal cell or an interneuron based on the spike waveform, firing rate, and autocorrelograms (15). The mice were equipped with an LED to track their head movements. Recordings were carried out in a home cage (W150×D150×H150 mm³) or a novelty box (a box of a different form of the home cage with novel objects). Slow-wave (SW) states were detected using the ratio of the power in the theta band (6–10 Hz) to the delta band (1–4 Hz) of the LFPs, followed by manual adjustment with the aid of visual inspection, time-resolved power spectra, and head movement data (Fig. S1). The manual adjustment was conducted to remove falsely detected short segments of data and epochs containing movement artifacts. To investigate the breakdown of SW states, another set of animals was used. Five C57BL/6J mice were implanted with tetrodes into the hippocampus and the prefrontal cortex for chronic LFP recordings and with stainless-steel wires into the neck muscles for electromyogram (EMG) recordings. Each LFP electrode consisted of 6 independent tetrodes and was made of a 17-μm-wide polyimide-coated platinum-iridium (90/10%) wire, the tip of which was plated with platinum to lower electrode impedances to 150–300 kΩ. The electrodes were stereotaxically implanted above the hippocampus (1.9 mm posterior and 1.7 mm lateral to bregma) and the frontal cortex (1.65 mm anterior and 0.3 mm lateral to bregma). An incision was made at the incised neck area, and the EMG electrode wire was sutured to the dorsal neck muscles. A ground/reference electrode was placed on the cerebellum, and a recording device was secured to the skull using stainless steel screws and dental cement. Then, the LFP electrodes were advanced to the targeted brain regions for at least one week after the surgery. Recordings were sampled at 2 kHz and filtered between 0.1 and 500 Hz. To monitor the rat's moment-to-moment position, their infrared signal was tracked at 15 Hz using a video camera attached to the ceiling. Awake immobility periods were detected semi-automatically based on EMG. For field excitatory postsynaptic potential (fEPSP) recordings, tungsten bipolar electrodes were implanted to stimulate the CA1 stratum radiatum. A 100-μs duration pulse was given every 20 s. The stimulus intensity was set to the intensity that resulted in an fEPSP with a slope 30–50% of the maximum, ranging between 60–90 μA.

For place cell identification, the recording arena was divided into bins of approximately $2 \times 2 \text{ cm}^2$ to generate spike count maps for each unit and an occupancy map (time spent by the animal in each bin). All maps were then smoothed by convolution with a Gaussian kernel with a standard deviation equal to one bin width. Finally, spatial rate maps were generated by normalizing the smoothed spike count maps by the smoothed occupancy map. Cells that showed remapping between the sessions were excluded from the analysis (34).

Real-time feedback delivery of light stimulation with the optogenetic technique

We used transgenic mice that expressed ChR2 (35) under the SOM promoter. We chose these mice because oriens-lacunosum moleculare (O-LM) interneurons in the CA3 region are more silent during sharp waves/ripples (SWRs) than other subtypes of interneurons (36) and thus are expected to efficiently suppress SWRs upon artificial activation (15). One or more optical fibers coupled with blue laser diodes (450 nm) were attached to a microdrive parallel to the silicon probes (Buzsaki32 or A4 \times 8) (37) so that the tip of the optic fiber could be placed in the CA3 pyramidal cell layer and the silicon probes in the CA1 pyramidal cell layer. The light power was set to 5–20 mW at the end of the fiber. A single channel from the middle of the CA1 pyramidal cell layer was selected for real-time processing by a programmable digital signal processor running at 25 kHz. The root mean square (RMS) of the bandpass filtered (140–250 Hz) signal was computed in two running windows, long (2 s; RMS1) and short (8 ms; RMS2). Ripples were defined as events with an RMS2 exceeding $4 \times \text{RMS1}$ for at least 8 ms, enabling the reliable online detection of the majority of ripples during their two or three cycles (confirmed by *post hoc* offline detection). Light stimulation was applied either under light (detection and stimulation) conditions or delayed (detection and 80-to-120-ms-delayed stimulation) conditions. The optogenetic stimulation was delivered 23 ± 12 ms after the onset of the SWR. When the false stimulation rate was estimated using local field potential (LFP) traces of the Sham sessions in which no light stimulation was immediately applied upon SWR detection, the false positive illumination rate $19.2 \pm 1.0\%$, whereas the false negative rate was $2.3 \pm 1.8\%$. The false-positive events were typically due to muscle movement artifacts. For the *in vitro* experiments, we used a custom-built routine running a script that read the signal from an amplifier. When the amplitude of the LFP crossed a manually set value, a light illumination was triggered through a digital signal with a modifiable delay and duration. Light was applied at powers of 0.05–0.2 mW.

Slice preparations

Wild-type, SOM::ChR2-EYFP, Thy1-mGFP, or Arc-dVenus transgenic C57BL/6J mice of either sex (3 weeks old) were placed in a novel chamber (280 mm wide, 300 mm long, 250 mm high) and were allowed to explore for 30 min. The mice were deeply anesthetized with diethyl ether and decapitated. The brains were removed quickly, and oblique or horizontal hippocampal slices (400 μm thick) were prepared using a vibratome in ice-cold, oxygenated cutting solution consisting of (in mM) 222.1 sucrose, 27 NaHCO_3 , 1.4 NaH_2PO_4 , 2.5 KCl, 1 CaCl_2 , 7 MgSO_4 , and 0.5 ascorbic acid (16). The slices were allowed to recover for at least 60 min and then submerged in a chamber filled

with oxygenated aCSF at 35–37°C. The aCSF consisted of (in mM) 127 NaCl, 1.6 KCl, 1.24 KH₂PO₄, 1.3 MgSO₄, 2.0 CaCl₂, 26 NaHCO₃, and 10 D-glucose for recordings (38).

In vitro electrophysiology

The slices were transferred to a recording chamber continuously perfused with aCSF at 32–33°C. The stimuli were delivered through a tungsten electrode, and fEPSPs were recorded using glass pipettes filled with aCSF or an 8×8 planar multi-electrode array (electrode size: 50×50 μm; inter-polar interval: 150 μm). The electrodes were carefully placed in the CA1 stratum radiatum within a distance of 100 μm from the pyramidal cell layer. A 100-μs pulse was given every 30 s. The stimulus intensity was set to result in an fEPSP with a slope of approximately 30% of the maximum fEPSP slope, ranging between 30–70 μA. Electrophysiological data were acquired using pCLAMP 10. The signals were low-pass filtered at 2 kHz and digitized at 20 kHz. The changes in fEPSP slope were expressed as percent changes in the initial slope relative to the mean slope during the baseline period. SWRs and multiunits were recorded using borosilicate glass pipettes (1–2 MΩ) filled with aCSF. The traces were bandpass filtered between 2 and 30 Hz for the LFP and were high-pass filtered at 300 Hz for multiunit recordings. Then, SWRs were detected at a threshold of 5× s.d. of the baseline noise. The detected events were visually scrutinized and manually rejected if they were erroneously detected. SWRs with event durations of less than 30 ms were also discarded because these events were typically artifacts. Because SWRs lasted for approximately 100 ms, we defined the activity that occurred within 100 ms before and after the SWR peak time as SWR-relevant activity by considering video frame jitters. In the experiments depicted in Fig. S6 and S8, to ensure that the tissue had recovered from slicing, we waited until the slice preparations began to emit SWRs at an event frequency of at least 0.8 Hz before beginning recordings. Then, the SWR event frequency gradually increased and peaked before the spontaneous decrease observed in SWR-emitting slices. Thus, for each slice, the time of the maximal SWR event frequency was defined as time 0 min, to which individual data were aligned for normalization.

Immunohistochemistry

The mice were anesthetized with isoflurane and perfused transcardially with cold phosphate-buffered saline (PBS; 1.47×10⁻³ M KH₂PO₄, 8.10×10⁻³ M Na₂HPO₄·12H₂O, 2.68×10⁻³ M KCl, 1.37×10⁻¹ M NaCl) followed by 4% paraformaldehyde. The brain samples were post-fixed with 4% paraformaldehyde for 4 h at 4°C and subsequently immersed in 15% and 30% sucrose for 24 h at 4°C. The brain area including the hippocampus was coronally sectioned at a thickness of 40 μm using a cryostat at -24°C. The sections were permeabilized for 30 min at room temperature in PBS with 0.3% Triton X-100 and 10% goat serum and incubated with the anti-GFP primary antibody (Chicken, 1:1000; #ab13970, Abcam, Cambridge, UK) in PBS with 0.3% Triton X-100 and 10% goat serum overnight at room temperature. After rinsing with PBS, the samples were incubated with a secondary antibody conjugated with Alexa Fluor dyes (Goat, 1:500; Invitrogen, Gaithersburg, MD, USA) and NeuroTrace 435/455 blue-fluorescent Nissl stain (1:500; #N21479, Thermo Fisher Scientific, Rockford, IL, USA) in PBS with 10% goat serum for 4 h at room temperature. After the samples were rinsed with PBS,

they were mounted with Permafluor (#TA-030-FM, Thermo Fisher Scientific, Rockford, IL, USA). Images were acquired using a FV1200 confocal system under a 20× objective.

Calcium imaging

Functional multineuron calcium imaging was conducted locally by loading cells with Fura-2AM, which can detect single spikes. Fura-2AM was dissolved in DMSO containing 10% Pluronic F-127 to yield a concentration of 200 μM . Immediately before use, this solution was diluted ten-fold with aCSF and loaded into pipettes (3–5 M Ω). The tip of the pipette was inserted into an acute horizontal slice, and a pressure of 50–60 hPa was applied for 3–5 min using a 10-ml syringe pressurizer. Fluorophores were excited at 405 nm with a laser diode and visualized using 507-nm-long pass emission filters. Videos were recorded for 3 min at 50 frames/s using a 16× objective (0.8 numerical aperture), a spinning-disk confocal microscope, and a cooled CCD camera or a CMOS embedded in an upright microscope. The fluorescence change was measured as $(F_t - F_0)/F_0$, where F_t is the fluorescence intensity at time t , and F_0 is the background fluorescence intensity between -10 to 10 s relative to t . Using a principal component analysis and a support vector machine optimized to calcium imaging, spike-elicited calcium transients were semiautomatically detected with a custom-written program in Visual Basic (38). Baseline noise was removed using the Okada filter (39). To examine the effect of D-AP5 perfusion on spontaneous neuronal activity, baseline activity was recorded for 3 min, and then 50 μM D-AP5 was bath-applied. Activity during the D-AP5 perfusion was recorded from 40 min to 43 min after the initiation of the perfusion. dVenus was excited at 488 nm and visualized using a 520/535-nm bandpass emission filter after 2 h of recording sessions. The response probability of individual dVenus(+) and dVenus(-) neurons was compared between 0–3 min and 40–43 min. The mean probability that a given cell exhibited a calcium transient during a single SWR event was defined as the SW participation probability of the cell.

Two-photon imaging

The dendrites of CA1 pyramidal cells in slices prepared from Thy1-GFP mice were imaged using a two-photon laser-scanning microscope. Fluorophores were excited at 900 nm, and fluorescence images were collected through a water-immersion 25× objective lens (1.05 NA). The first set of images was taken 5 min after the SWR event frequency reached 0.80 Hz. Regions of dendrites (usually second or third order branches) that had 5–34 spines were selected and time-lapse imaged at a higher magnification (optical zoom = 5×). Images were taken every 15 min at a resolution of 512×512 or 256×256 pixels. The spine head volume was estimated as $4\pi(\phi/2)^3/3$, in which ϕ represents the head width of the spine (40). The head width was measured from the maximum spine area across a series of Z-step images (0.5 μm steps). The distance from the center of gravity of the spine head to the stem dendrite was measured as the spine neck length. Spines were classified into stubby, thin, or mushroom based on their length, spine head diameter, and neck diameter using IMARIS software (41, 42). The data were analyzed by experimenters who were unaware of the experimental conditions

Data analysis

Values are reported as the mean with individual data points or mean \pm s.e.m., except for the data in Fig. S8B and S8C, which used geometric mean \pm s.e.m. and whisker plots composed of the median (central line in the box), ranges between the 25th and 75th percentile (box) and between the 10th and 90th percentiles (whiskers). Data analyses were performed in a blind fashion.

Primary numerical data sets is available online (URL: http://ikegaya.jp/data/norimoto_science2018/)

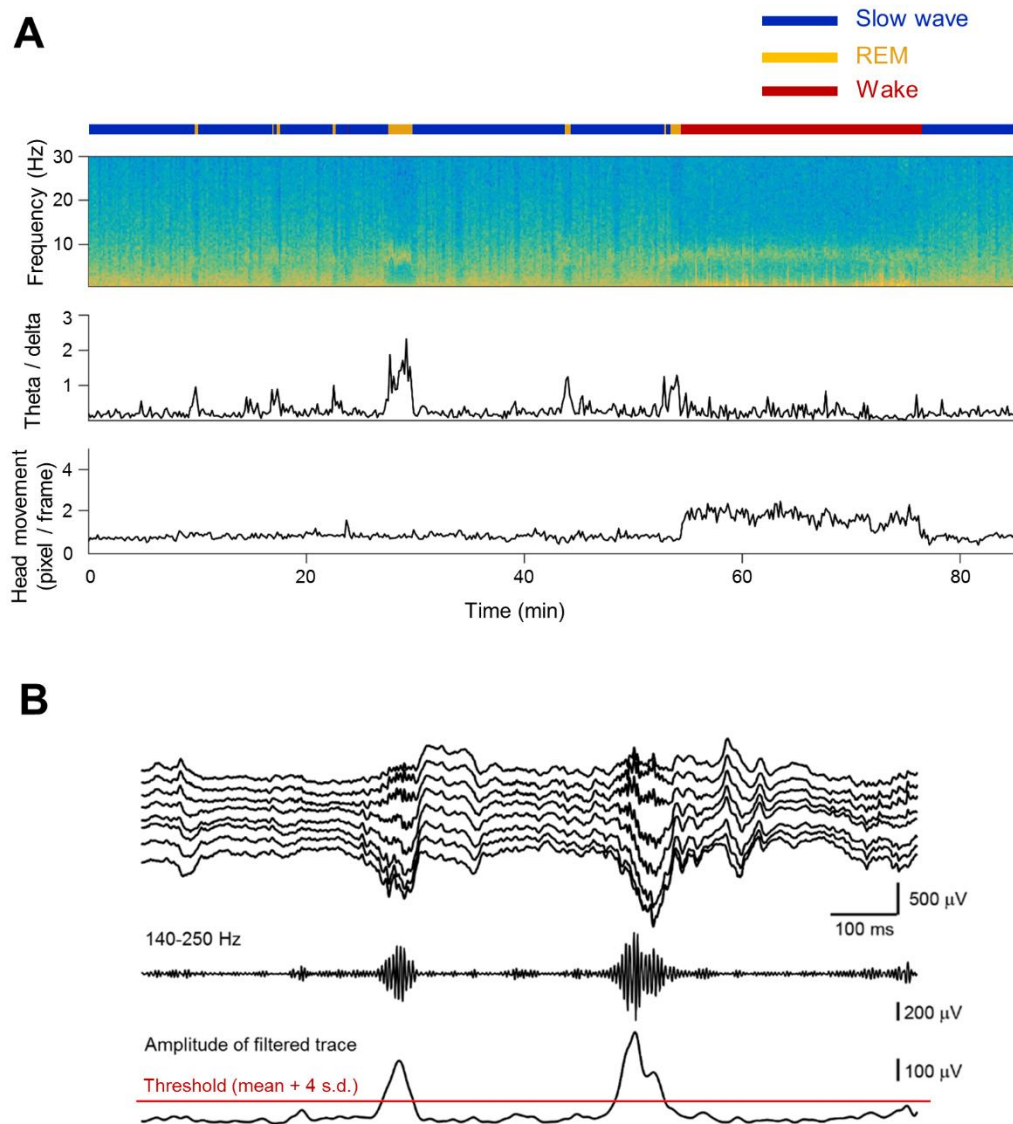


Fig. S1. Classification of brain states. **(A)** Time-resolved power spectrum of an LFP trace recorded from the hippocampal CA1 region. The two bottom plots indicate the theta/delta ratio and head movements, which were used to define brain states, *i.e.*, slow-wave state, rapid eye movement (REM) state, and waking state. **(B)** The threshold for SWR detection was set to $4\times$ s.d. above the mean power. Top, raw LFP traces recorded from the CA1 region; Middle, a trace filtered in a ripple-frequency (140–250 Hz) band; Bottom, a trace representing the LFP envelope amplitude (power).

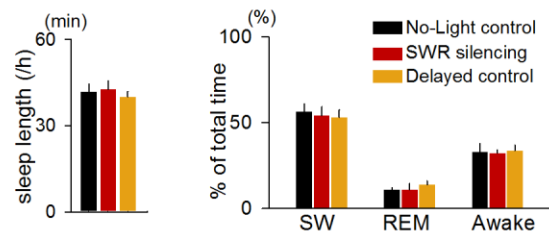


Fig. S2. SWR silencing does not affect sleep quality. Left: the total sleep length during the 7-h SWR silencing period did not differ among the groups. $P = 0.79$, $F_{2,13} = 0.236$, one-way ANOVA. Right: the percentages of SW, REM, and awake states did not differ during SWR silencing. SW: $P = 0.89$, $F_{2,15} = 0.12$, REM: $P = 0.68$, $F_{2,15} = 0.40$, Awake: $P = 0.97$, $F_{2,15} = 0.035$, one-way ANOVA.

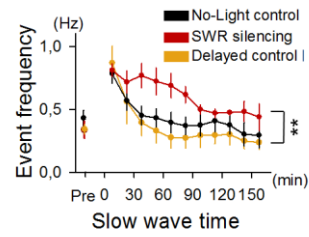


Fig. S3. The SWR-silenced group shows higher SWR event frequencies than the delayed control group throughout the recording time. Silencing vs. no-light control: $** P = 1.2 \times 10^{-5}$, $F_{1,106} = 21.2$, Silencing vs. delayed control: $** P = 6.5 \times 10^{-8}$, $F_{1,81} = 36.8$, two-way ANOVA. $n = 6-7$ mice.

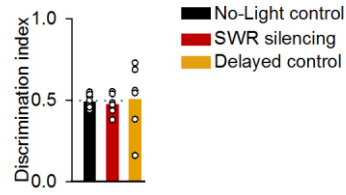


Fig. S4. No behavioral differences were observed in the encoding phase of the object-place recognition task. The percentage of time spent exploring two identical objects did not differ between the SWR silencing, the delayed control, and the no-light control ($P = 0.54$, $H_2 = 1.23$, Kruskal-Wallis one-way ANOVA on ranks, $n = 6-7$ mice).

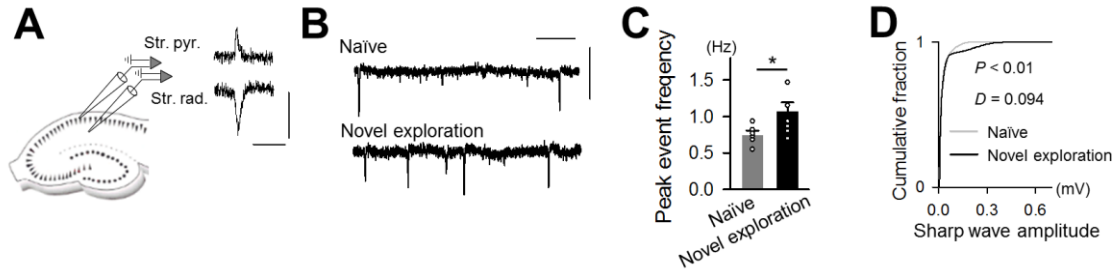


Fig. S5. Spatial exploration increases the event frequency of SWRs in hippocampal slice preparation. **(A)** SWRs were recorded from the CA1 stratum radiatum and the pyramidale. Scale bars = 100 ms and 0.1 mV. **(B)** Representative raw LFP traces recorded from the stratum radiatum of the hippocampal slices prepared from naïve mice (top) and mice that had explored a novel environment for 30 min (bottom). Scale bars = 1 s and 0.1 mV. **(C)** Slices prepared from mice that had experienced spatial exploration exhibited higher SWR event frequencies than slices from naïve mice. $*P = 0.043$, $t_{10} = -1.90$, one-tailed t -test. $n = 6$ slices from 6 mice. **(D)** Slices prepared from mice that had experienced spatial exploration exhibited higher SWR amplitudes than slices from naïve mice. $P = 4.6 \times 10^{-32}$, $D_{22195} = 0.094$, Kolmogorov-Smirnov test. $n = 5467$ and 16731 events.

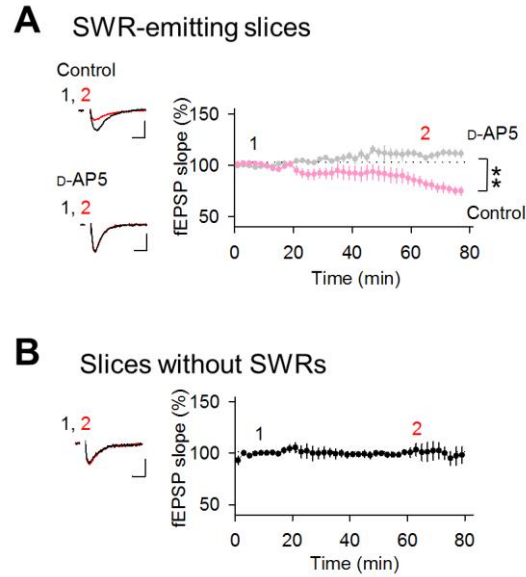


Fig. S6. Spontaneous depression of fEPSPs in SWR-emitting slices. **(A)** SWRs and fEPSPs were recorded in the continuous presence or absence of 50 μ M D-AP5 from the CA1 stratum radiatum of hippocampal slices prepared from mice that had explored a novel environment for 30 min. A stimulating electrode was placed on the CA1 stratum radiatum. The fEPSP slopes were normalized to the 20-min baseline values. The insets show typical fEPSP traces at the times indicated by 1 and 2. Scale bars = 10 ms and 50 μ V. The fEPSP slopes gradually declined over time but did not decline in the presence of D-AP5. $**P = 3.0 \times 10^{-41}$, $F_{1,240} = 270.8$, two-way ANOVA, $n = 5$ each. **(B)** LTD was not induced in conventional slices that did not emit SWRs. $n = 4$ slices. Scale bars = 10 ms and 50 μ V.

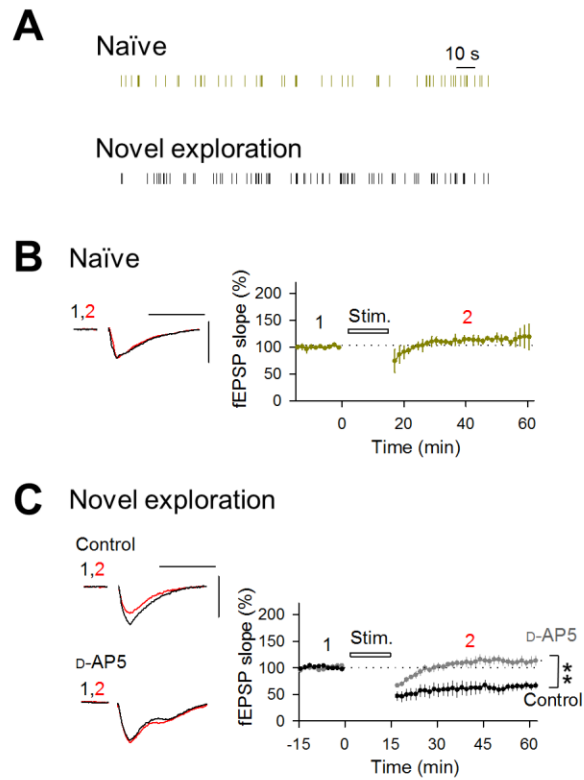


Fig. S7. Repetitive stimulation patterned from *in vivo* SWR timings leads to long-term depression. **(A)** Examples of stimulation patterns that were applied to the Schaffer collaterals (parts). These SWR timings were obtained for 15 min during *in vivo* SW states of naïve mice and mice that had explored a novel environment for 30 min. **(B)** Stimulation patterned from SWR timings in naïve mice did not induce LTD in conventional slices that did not emit SWRs ($n = 3$ slices). **(C)** Stimulation patterned from SWR timings after spatial explorations induced LTD, which was blocked by a bath application of $50 \mu\text{M}$ D-AP5. $**P = 2.5 \times 10^{-46}$, $F_{1,376} = 271.7$, two-way ANOVA, $n = 5$ slices each. The insets in each panel show typical fEPSP traces at times 1 and 2. Scale bars = 20 ms and 1 mV.

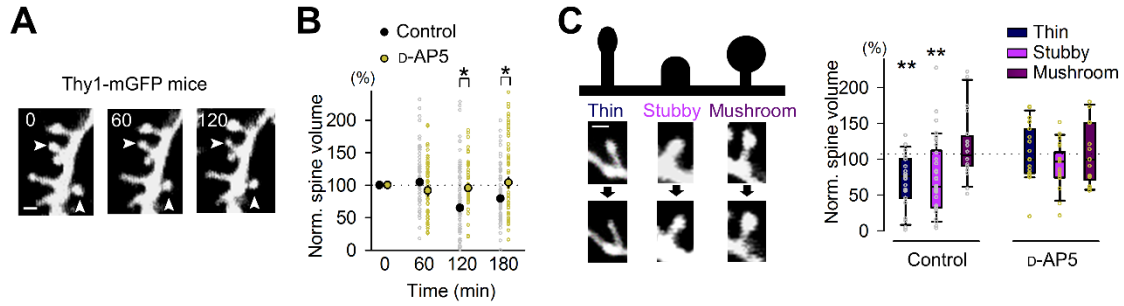


Fig. S8. SWR-emitting slices exhibit NMDAR-dependent spontaneous spine shrinkage. (A) Time-lapse two-photon imaging of dendritic spines on an apical dendrite of a CA1 pyramidal neuron in a slice prepared from a Thy1-GFP mouse. Arrowheads indicate spines that shrank. (B) Percentage changes in the volume of the spine heads during SWRs in the presence or absence of 50 μM D-AP5. Time 0 is aligned at the time of the maximal frequencies of SWR events. 120 min: $*P = 0.014$, $Z = 2.47$, 180 min: $*P < 1.0 \times 10^{-30}$, $Z = 8.24$, Wilcoxon signed rank test, Control: $n = 77$ spines from 4 slices from 4 mice; D-AP5: $n = 55$ spines of 5 slices from 5 mice. (C) Thin and stubby types but not mushroom types spontaneously shrank at 120 min. D-AP5 prevented spine shrinkage. Scale bar = 1 μm . Thin: $**P = 2.0 \times 10^{-5}$, $Z = 4.11$; Stubby: $**P = 5.9 \times 10^{-7}$, $Z = 4.86$, one-sample signed rank test, Control: $n = 20$ –31 spines, D-AP5: $n = 14$ –21 spines

References and Notes

1. V. V. Vyazovskiy, C. Cirelli, M. Pfister-Genskow, U. Faraguna, G. Tononi, Molecular and electrophysiological evidence for net synaptic potentiation in wake and depression in sleep. *Nat. Neurosci.* **11**, 200–208 (2008). [doi:10.1038/nn2035](https://doi.org/10.1038/nn2035) [Medline](#)
2. R. Huber, H. Mäki, M. Rosanova, S. Casarotto, P. Canali, A. G. Casali, G. Tononi, M. Massimini, Human cortical excitability increases with time awake. *Cereb. Cortex* **23**, 332–338 (2013). [doi:10.1093/cercor/bhs014](https://doi.org/10.1093/cercor/bhs014) [Medline](#)
3. G. Tononi, C. Cirelli, Sleep and synaptic homeostasis: A hypothesis. *Brain Res. Bull.* **62**, 143–150 (2003). [doi:10.1016/j.brainresbull.2003.09.004](https://doi.org/10.1016/j.brainresbull.2003.09.004) [Medline](#)
4. G. Tononi, C. Cirelli, Sleep and the price of plasticity: From synaptic and cellular homeostasis to memory consolidation and integration. *Neuron* **81**, 12–34 (2014). [doi:10.1016/j.neuron.2013.12.025](https://doi.org/10.1016/j.neuron.2013.12.025) [Medline](#)
5. A. K. Lee, M. A. Wilson, Memory of sequential experience in the hippocampus during slow wave sleep. *Neuron* **36**, 1183–1194 (2002). [doi:10.1016/S0896-6273\(02\)01096-6](https://doi.org/10.1016/S0896-6273(02)01096-6) [Medline](#)
6. V. Ego-Stengel, M. A. Wilson, Disruption of ripple-associated hippocampal activity during rest impairs spatial learning in the rat. *Hippocampus* **20**, 1–10 (2010). [Medline](#)
7. G. Girardeau, K. Benchenane, S. I. Wiener, G. Buzsáki, M. B. Zugaro, Selective suppression of hippocampal ripples impairs spatial memory. *Nat. Neurosci.* **12**, 1222–1223 (2009). [doi:10.1038/nn.2384](https://doi.org/10.1038/nn.2384) [Medline](#)
8. G. M. van de Ven, S. Trouche, C. G. McNamara, K. Allen, D. Dupret, Hippocampal offline reactivation consolidates recently formed cell assembly patterns during sharp wave-ripples. *Neuron* **92**, 968–974 (2016). [doi:10.1016/j.neuron.2016.10.020](https://doi.org/10.1016/j.neuron.2016.10.020) [Medline](#)
9. J. H. Sadowski, M. W. Jones, J. R. Mellor, Sharp-wave ripples orchestrate the induction of synaptic plasticity during reactivation of place cell firing patterns in the hippocampus. *Cell Rep.* **14**, 1916–1929 (2016). [doi:10.1016/j.celrep.2016.01.061](https://doi.org/10.1016/j.celrep.2016.01.061) [Medline](#)
10. E. V. Lubenov, A. G. Siapas, Decoupling through synchrony in neuronal circuits with propagation delays. *Neuron* **58**, 118–131 (2008). [doi:10.1016/j.neuron.2008.01.036](https://doi.org/10.1016/j.neuron.2008.01.036) [Medline](#)
11. L. L. Colgin, D. Kubota, Y. Jia, C. S. Rex, G. Lynch, Long-term potentiation is impaired in rat hippocampal slices that produce spontaneous sharp waves. *J. Physiol.* **558**, 953–961 (2004). [doi:10.1113/jphysiol.2004.068080](https://doi.org/10.1113/jphysiol.2004.068080) [Medline](#)
12. O. Bukalo, E. Campanac, D. A. Hoffman, R. D. Fields, Synaptic plasticity by antidromic firing during hippocampal network oscillations. *Proc. Natl. Acad. Sci. U.S.A.* **110**, 5175–5180 (2013). [doi:10.1073/pnas.1210735110](https://doi.org/10.1073/pnas.1210735110) [Medline](#)
13. O. Eschenko, W. Ramadan, M. Mölle, J. Born, S. J. Sara, Sustained increase in hippocampal sharp-wave ripple activity during slow-wave sleep after learning. *Learn. Mem.* **15**, 222–228 (2008). [doi:10.1101/lm.726008](https://doi.org/10.1101/lm.726008) [Medline](#)
14. C. J. Behrens, L. P. van den Boom, L. de Hoz, A. Friedman, U. Heinemann, Induction of sharp wave-ripple complexes in vitro and reorganization of hippocampal networks. *Nat. Neurosci.* **8**, 1560–1567 (2005). [doi:10.1038/nn1571](https://doi.org/10.1038/nn1571) [Medline](#)

15. E. Stark, L. Roux, R. Eichler, Y. Senzai, S. Royer, G. Buzsáki, Pyramidal cell-interneuron interactions underlie hippocampal ripple oscillations. *Neuron* **83**, 467–480 (2014). [doi:10.1016/j.neuron.2014.06.023](https://doi.org/10.1016/j.neuron.2014.06.023) [Medline](#)
16. M. Mizunuma, H. Norimoto, K. Tao, T. Egawa, K. Hanaoka, T. Sakaguchi, H. Hioki, T. Kaneko, S. Yamaguchi, T. Nagano, N. Matsuki, Y. Ikegaya, Unbalanced excitability underlies offline reactivation of behaviorally activated neurons. *Nat. Neurosci.* **17**, 503–505 (2014). [doi:10.1038/nn.3674](https://doi.org/10.1038/nn.3674) [Medline](#)
17. G. L. Collingridge, S. J. Kehl, H. McLennan, Excitatory amino acids in synaptic transmission in the Schaffer collateral-commissural pathway of the rat hippocampus. *J. Physiol.* **334**, 33–46 (1983). [doi:10.1113/jphysiol.1983.sp014478](https://doi.org/10.1113/jphysiol.1983.sp014478) [Medline](#)
18. M. Matsuzaki, G. C. Ellis-Davies, T. Nemoto, Y. Miyashita, M. Iino, H. Kasai, Dendritic spine geometry is critical for AMPA receptor expression in hippocampal CA1 pyramidal neurons. *Nat. Neurosci.* **4**, 1086–1092 (2001). [doi:10.1038/nn736](https://doi.org/10.1038/nn736) [Medline](#)
19. M. Masugi-Tokita, E. Tarusawa, M. Watanabe, E. Molnár, K. Fujimoto, R. Shigemoto, Number and density of AMPA receptors in individual synapses in the rat cerebellum as revealed by SDS-digested freeze-fracture replica labeling. *J. Neurosci.* **27**, 2135–2144 (2007). [doi:10.1523/JNEUROSCI.2861-06.2007](https://doi.org/10.1523/JNEUROSCI.2861-06.2007) [Medline](#)
20. Q. Zhou, K. J. Homma, M. M. Poo, Shrinkage of dendritic spines associated with long-term depression of hippocampal synapses. *Neuron* **44**, 749–757 (2004). [doi:10.1016/j.neuron.2004.11.011](https://doi.org/10.1016/j.neuron.2004.11.011) [Medline](#)
21. O. Paulsen, T. J. Sejnowski, Natural patterns of activity and long-term synaptic plasticity. *Curr. Opin. Neurobiol.* **10**, 172–179 (2000). [doi:10.1016/S0959-4388\(00\)00076-3](https://doi.org/10.1016/S0959-4388(00)00076-3) [Medline](#)
22. M. Eguchi, S. Yamaguchi, In vivo and in vitro visualization of gene expression dynamics over extensive areas of the brain. *Neuroimage* **44**, 1274–1283 (2009). [doi:10.1016/j.neuroimage.2008.10.046](https://doi.org/10.1016/j.neuroimage.2008.10.046) [Medline](#)
23. D. Balduzzi, G. Tononi, What can neurons do for their brain? Communicate selectivity with bursts. *Theory Biosci.* **132**, 27–39 (2013). [doi:10.1007/s12064-012-0165-0](https://doi.org/10.1007/s12064-012-0165-0) [Medline](#)
24. S. S. Yoo, P. T. Hu, N. Gujar, F. A. Jolesz, M. P. Walker, A deficit in the ability to form new human memories without sleep. *Nat. Neurosci.* **10**, 385–392 (2007). [doi:10.1038/nn1851](https://doi.org/10.1038/nn1851) [Medline](#)
25. G. S. Lynch, T. Dunwiddie, V. Gribkoff, Heterosynaptic depression: A postsynaptic correlate of long-term potentiation. *Nature* **266**, 737–739 (1977). [doi:10.1038/266737a0](https://doi.org/10.1038/266737a0) [Medline](#)
26. R. M. Mulkey, R. C. Malenka, Mechanisms underlying induction of homosynaptic long-term depression in area CA1 of the hippocampus. *Neuron* **9**, 967–975 (1992). [doi:10.1016/0896-6273\(92\)90248-C](https://doi.org/10.1016/0896-6273(92)90248-C) [Medline](#)
27. S. M. Dudek, M. F. Bear, Homosynaptic long-term depression in area CA1 of hippocampus and effects of N-methyl-D-aspartate receptor blockade. *Proc. Natl. Acad. Sci. U.S.A.* **89**, 4363–4367 (1992). [doi:10.1073/pnas.89.10.4363](https://doi.org/10.1073/pnas.89.10.4363) [Medline](#)
28. L. de Vivo, M. Bellesi, W. Marshall, E. A. Bushong, M. H. Ellisman, G. Tononi, C. Cirelli, Ultrastructural evidence for synaptic scaling across the wake/sleep cycle. *Science* **355**, 507–510 (2017). [doi:10.1126/science.aah5982](https://doi.org/10.1126/science.aah5982) [Medline](#)

29. G. H. Diering, R. S. Nirujogi, R. H. Roth, P. F. Worley, A. Pandey, R. L. Huganir, Homer1a drives homeostatic scaling-down of excitatory synapses during sleep. *Science* **355**, 511–515 (2017). [doi:10.1126/science.aai8355](https://doi.org/10.1126/science.aai8355) [Medline](#)
30. M. R. Mehta, Cortico-hippocampal interaction during up-down states and memory consolidation. *Nat. Neurosci.* **10**, 13–15 (2007). [doi:10.1038/nn0107-13](https://doi.org/10.1038/nn0107-13) [Medline](#)
31. G. Feng, R. H. Mellor, M. Bernstein, C. Keller-Peck, Q. T. Nguyen, M. Wallace, J. M. Nerbonne, J. W. Lichtman, J. R. Sanes, Imaging neuronal subsets in transgenic mice expressing multiple spectral variants of GFP. *Neuron* **28**, 41–51 (2000). [doi:10.1016/S0896-6273\(00\)00084-2](https://doi.org/10.1016/S0896-6273(00)00084-2) [Medline](#)
32. S. Fujisawa, A. Amarasingham, M. T. Harrison, G. Buzsáki, Behavior-dependent short-term assembly dynamics in the medial prefrontal cortex. *Nat. Neurosci.* **11**, 823–833 (2008). [doi:10.1038/nn.2134](https://doi.org/10.1038/nn.2134) [Medline](#)
33. S. N. Kadir, D. F. Goodman, K. D. Harris, High-dimensional cluster analysis with the masked EM algorithm. *Neural Comput.* **26**, 2379–2394 (2014). [doi:10.1162/NECO_a_00661](https://doi.org/10.1162/NECO_a_00661) [Medline](#)
34. S. Leutgeb, J. K. Leutgeb, A. Treves, M. B. Moser, E. I. Moser, Distinct ensemble codes in hippocampal areas CA3 and CA1. *Science* **305**, 1295–1298 (2004). [doi:10.1126/science.1100265](https://doi.org/10.1126/science.1100265) [Medline](#)
35. E. S. Boyden, F. Zhang, E. Bamberg, G. Nagel, K. Deisseroth, Millisecond-timescale, genetically targeted optical control of neural activity. *Nat. Neurosci.* **8**, 1263–1268 (2005). [doi:10.1038/nn1525](https://doi.org/10.1038/nn1525) [Medline](#)
36. T. Klausberger, P. J. Magill, L. F. Márton, J. D. Roberts, P. M. Cobden, G. Buzsáki, P. Somogyi, Brain-state- and cell-type-specific firing of hippocampal interneurons in vivo. *Nature* **421**, 844–848 (2003). [doi:10.1038/nature01374](https://doi.org/10.1038/nature01374) [Medline](#)
37. S. Royer, B. V. Zemelman, M. Barbic, A. Losonczy, G. Buzsáki, J. C. Magee, Multi-array silicon probes with integrated optical fibers: Light-assisted perturbation and recording of local neural circuits in the behaving animal. *Eur. J. Neurosci.* **31**, 2279–2291 (2010). [doi:10.1111/j.1460-9568.2010.07250.x](https://doi.org/10.1111/j.1460-9568.2010.07250.x) [Medline](#)
38. H. Norimoto, M. Mizunuma, D. Ishikawa, N. Matsuki, Y. Ikegaya, Muscarinic receptor activation disrupts hippocampal sharp wave-ripples. *Brain Res.* **1461**, 1–9 (2012). [doi:10.1016/j.brainres.2012.04.037](https://doi.org/10.1016/j.brainres.2012.04.037) [Medline](#)
39. M. Okada, T. Ishikawa, Y. Ikegaya, A computationally efficient filter for reducing shot noise in low S/N data. *PLOS ONE* **11**, e0157595 (2016). [doi:10.1371/journal.pone.0157595](https://doi.org/10.1371/journal.pone.0157595) [Medline](#)
40. N. Takahashi, K. Kitamura, N. Matsuo, M. Mayford, M. Kano, N. Matsuki, Y. Ikegaya, Locally synchronized synaptic inputs. *Science* **335**, 353–356 (2012). [doi:10.1126/science.1210362](https://doi.org/10.1126/science.1210362) [Medline](#)
41. A. Peters, I. R. Kaiserman-Abramof, The small pyramidal neuron of the rat cerebral cortex. The perikaryon, dendrites and spines. *Am. J. Anat.* **127**, 321–355 (1970). [doi:10.1002/aja.1001270402](https://doi.org/10.1002/aja.1001270402) [Medline](#)
42. K. M. Harris, F. E. Jensen, B. Tsao, Three-dimensional structure of dendritic spines and synapses in rat hippocampus (CA1) at postnatal day 15 and adult ages: Implications for the maturation of synaptic physiology and long-term potentiation. *J. Neurosci.* **12**, 2685–2705 (1992). [Medline](#)

as anti-programmed cell death protein 1 (PD-1), anti-PD-1 ligand 1 (PD-L1), or other T cell-based therapies, including the adoptive transfer of engineered T cells to further enhance T cell activation. These combinations would not only enhance both CD8⁺ T cell and NK cell activation against cancer cells but, in addition, broaden the spectrum of tumor cells that can be attacked.

MICA and MICB expression has been reported in healthy individuals in barrier tissues such as the gut. It is unknown whether these cells also shed NKG2D ligands. Expression and stabilization of MICA and MICB in these tissues could cause excessive inflammation resulting from aberrant immune cell activation and might lead to serious side effects. Additionally, circulating monocytes and tumor-infiltrating myeloid cells in some cancer patients express MICB. Activated T cells can express NKG2D ligands as well (14). Moreover, under homeostatic conditions, NKG2D ligands were detected on mouse endothelial cells and might modulate NK cell function (15). Whether NKG2D ligands on myeloid cells, T cells, and endothelial cells are also stabilized by the MICA-MICB mAb, potentially promoting inflammation, has not been addressed. Undoubtedly, future studies are needed to provide a comprehensive analysis of MICA and MICB expression in homeostatic conditions and during disease.

Bispecific mAbs targeting additional antitumor effector cells, such as CD3⁺ T cells (which infiltrate solid tumors at higher numbers than NK cells), to MICA- and MICB-bearing tumors could be generated. Moreover, the MICA-MICB mAb could also be engineered into T cells or NK cells for adoptive cell transfer, potentially resulting in efficient tumor cell targeting, provided there is no toxic off-target cell killing. Ferrari de Andrade *et al.* reveal an innovative approach to counteract a major mechanism of cancer immune escape from NK cell recognition that, if safe in patients, harbors high potential and versatility for future clinical application. ■

REFERENCES

1. L. Ferrari de Andrade *et al.*, *Science* **359**, 1537 (2018).
2. S. Bauer *et al.*, *Science* **285**, 727 (1999).
3. J. Wu *et al.*, *Science* **285**, 730 (1999).
4. L. L. Lanier *et al.*, *Cancer Immunol. Res.* **3**, 575 (2015).
5. E. P. von Strandmann *et al.*, *Blood* **107**, 1955 (2006).
6. J. Steinbacher *et al.*, *Int. J. Cancer* **136**, 1073 (2015).
7. C. Godbersen *et al.*, *Mol. Cancer Ther.* **16**, 1335 (2017).
8. H. R. Salih *et al.*, *J. Immunol.* **169**, 4098 (2002).
9. V. Groh *et al.*, *Nature* **419**, 734 (2002).
10. N. Nausch *et al.*, *Oncogene* **27**, 5944 (2008).
11. M. Della Chiesa *et al.*, *Blood* **108**, 4118 (2006).
12. L. Chiossone *et al.*, *Sem. Immunol.* **31**, 55 (2017).
13. A. I. Roberts *et al.*, *J. Immunol.* **167**, 5527 (2001).
14. C. Cerboni *et al.*, *Blood* **113**, 2955 (2009).
15. T. W. Thompson *et al.*, *eLife* **6**, e30881 (2017).

10.1126/science.aat2184

NEUROSCIENCE

Making room for new memories

Clearing neuronal networks from transient memory engrams during sleep consolidates memories

By **Andreas Draguhn**

What are our memories made of? Plato suggested imagining a block of wax in our soul, where perceptions and thoughts leave impressions that we can remember as long as they have not been erased. This historic metaphor captures the transience of some memories and the stability of others, and it illustrates the brain's plasticity. The mechanisms of memory formation and retention remain a key question in neuroscience. Groundbreaking work on the rodent hippocampus (a network in the temporal lobe) revealed that certain neurons form transiently stable representations of places (1). Hence, this brain region has become an important focus for

“...how can we remember an almost infinite number of items with the limited storage capacity of the hippocampus?...neuronal activity during sleep plays a major role...”

studying spatial memory (or engram) formation. It also serves as an experimentally accessible proxy for declarative (knowledge) and episodic (experience) memory in humans, which involves the same brain structures and mechanisms. However, how can we remember an almost infinite number of items with the limited storage capacity of the hippocampus? There is good evidence that relevant representations are transferred to neocortical networks before forming long-lasting engrams. The hippocampus is then reset for acquisition of new memories. Studies in animals (2) and humans (3) show that neuronal activity during sleep plays a major role in these processes. The underlying mechanisms,

Institute of Physiology and Pathophysiology, Heidelberg University, Im Neuenheimer Feld 326, 69120 Heidelberg, Germany. Email: andreas.draguhn@physiologie.uni-heidelberg.de

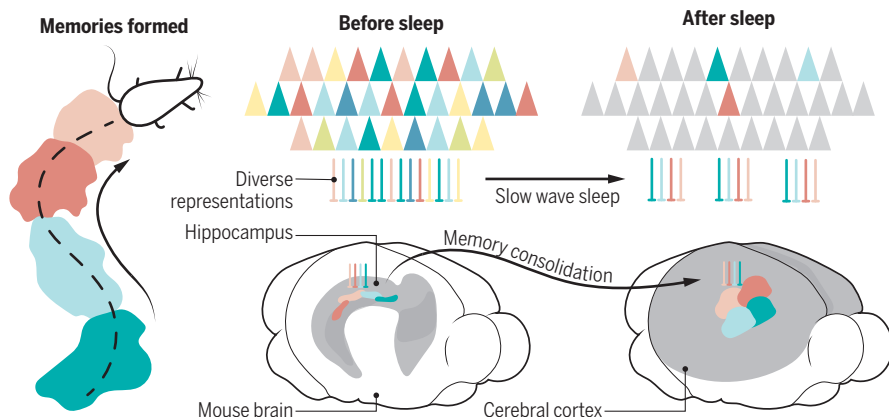
however, have remained mostly enigmatic. On page 1524 of this issue, Norimoto *et al.* (4) show how sleep-associated activity patterns induce “negative” neuronal plasticity in the hippocampus, erasing remote memories. A previous, related paper by Khodagholy *et al.* (5) reveals similar activity patterns in the neocortex, which, hence, may mediate long-term consolidation of transient engrams at their final location.

Norimoto *et al.* show that excitatory synapses between hippocampal neurons are weakened by sharp wave-ripple (SWR) complexes, patterns of coordinated network activity that typically occur during sleep (6) (see the figure). Surprisingly, neurons contributing to recently acquired engrams are excluded from this weakening and remain stably active. Behavioral tests suggest that this mechanism supports the formation of new memories, in line with the idea that the hippocampal memory system must be regularly cleared. This requires, however, that “old” memories (if relevant) must be stored elsewhere, fostering the idea of engram transfer from the hippocampus to the neocortex (7).

The representation of spatial contexts in hippocampal networks involves three major mechanisms. First, special neurons called “place cells” are selectively activated when the animal is in a certain spot of its environment (1). Second, exploring an environment strengthens the coupling of sequentially activated place cells, which then form neuronal ensembles representing the spatial experience (8). Third, coherent membrane potential oscillations of all local neurons provide a common time frame for coordinating the activation of coupled neurons (9). The resulting spatio-temporal activity patterns form transiently stable representations of spatial experience. A key observation from multineuronal recordings in rats links such coactive neuronal ensembles to memory consolidation: Sequences of place cell activity that were formed during spatial exploration are replayed in the same order during phases of immobility or slow-wave sleep (2). This sleep state, better known as deep or non-REM (rapid eye movement) sleep, is exactly the phase where humans stabilize recently formed memories (3). Compared to memory acquisition, however, replay of

Processing of engrams in the rodent brain

Firing of place cells during spatial exploration leads to the formation of coactive neuronal ensembles. During subsequent sleep, engrams of old ensembles are erased, which increases the distinction of newly formed ensembles. Memory consolidation occurs through hippocampal-cortical cross-talk, indicated by SWR-like activity patterns during sleep.



activity sequences occurs on top of a much faster pattern of network oscillations—hippocampal SWRs.

Norimoto *et al.* first confirmed two properties of slow-wave sleep in mice: Synaptic coupling strength between hippocampal neurons declines (10), and hippocampal networks produce spontaneous SWR activity (6). They then asked whether there is a causal link between both phenomena, using an elegant optogenetic closed-loop technique to silence neuronal activity during SWRs with pulses of light. Indeed, aborting the patterns prevented the decay of synaptic coupling and, at the same time, blocked hippocampus-dependent spatial memory formation. How do slow-wave sleep, SWRs, and the related synaptic plasticity support spatial memory? Recordings from multiple single neurons revealed that the decline in activity was selective for those place cells that represent old, well-known environments, whereas recently formed place cells remained fully active. Reducing the strength of recently unchanged synapses may prevent saturation of synaptic strength and ensure homeostasis of excitability in the network (10). It separates newly formed ensembles from old, established engrams (4) and clears the stage for “positive” synaptic plasticity during future experiences.

The underlying cellular and molecular mechanisms involve changes in dendritic spine size and depend on activation of NMDA (*N*-methyl-*D*-aspartate) receptors, both typical for activity-dependent synaptic plasticity (11). At present, it remains unclear how newly potentiated synapses (or memory-relevant neurons) are distinguished from established connections (or

memory-irrelevant neurons). The findings by Norimoto *et al.* and the precise timing of neuronal activity during SWR events (6) suggest a role for spike-timing-dependent plasticity (11)—lasting changes in synaptic strength upon near-coincident activation of pre- and postsynaptic neurons.

Thus, as time progresses, old impressions are progressively erased from Plato’s block of wax, avoiding confusion by superimposed engrams. But where and how are representations preserved to form long-lived memories for the many places and objects we (and rodents) know? The prevailing view is that during SWRs, replayed neuronal activity patterns are transferred from the hippocampus into distributed

“The findings also underline the important role of slow-wave sleep for the consolidation of spatial (and declarative) memories.”

neocortical networks (7). There, some unknown process of plasticity is induced that forms stable representations. Indeed, hippocampal SWRs coincide with defined patterns of sleep-related neocortical network activity (12, 13). However, the precise nature and location of neocortical long-term engrams remain elusive. Important progress comes from Khodagholy *et al.* They used dense, large-scale electrode arrays to study multineuronal activity patterns in rats subjected to a hippocampus-dependent memory task. With this de-

vice, they detected fast oscillations in the “ripple” frequency band (typical for SWRs) in several circumscribed neocortical areas (see the figure). Neocortical ripples are restricted to prefrontal or parietal “association” cortices, i.e., areas with rich intracortical connections that are involved in cognitive functions like action planning and spatial navigation. The pattern occurs coincidentally with hippocampal SWRs, and coupling between both areas is increased by previous spatial learning episodes. Given that the highly coincident neuronal activation during SWRs facilitates synaptic potentiation (14), neocortical ripples are a strong candidate mechanism for the induction of long-lasting engrams. The findings also underline the important role of slow-wave sleep for the consolidation of spatial (and declarative) memories.

Together, the two studies mark considerable progress in understanding the network-level mechanisms of spatial memory formation. Both groups made elegant use of recent methodological advances: Khodagholy *et al.* performed massively parallel recordings from large numbers of neurons, establishing new correlations between multineuronal patterns, vigilance states, and behavioral performance. Norimoto *et al.* used an interventionist approach to unravel causal relationships between network activity, synaptic plasticity, and memory. It should be kept in mind, however, that we are far from a complete reconstruction of all elements and causal interactions linking molecular events, neuronal coupling, local network oscillations, whole-brain information processing, memory formation, and behavior—provided this can ever be achieved (15). Crucial future steps include identifying the (sub)cellular events that couple neurons within ensembles, elucidating the mechanisms that determine the transience or stability of engrams, and pinpointing the location and nature of neocortical memory-related ensembles. ■

REFERENCES

1. J. O’Keefe, J. Dostrovsky, *Brain Res.* **34**, 171 (1971).
2. A. K. Lee, M. A. Wilson, *Neuron* **36**, 1183 (2002).
3. L. Marshall *et al.*, *Nature* **444**, 610 (2006).
4. H. Norimoto *et al.*, *Science* **359**, 1524 (2018).
5. D. Khodagholy *et al.*, *Science* **358**, 369 (2017).
6. G. Buzsáki *et al.*, *Science* **256**, 1025 (1992).
7. G. Buzsáki, *Hippocampus* **25**, 1073 (2015).
8. L. M. Frank *et al.*, *Hippocampus* **16**, 775 (2006).
9. G. Buzsáki, A. Draguhn, *Science* **304**, 1926 (2004).
10. V. V. Vyazovskiy *et al.*, *Nat. Neurosci.* **11**, 200 (2008).
11. Q. Zhou *et al.*, *Neuron* **44**, 749 (2004).
12. A. G. Siapas, M. A. Wilson, *Neuron* **21**, 1123 (1998).
13. A. Sirota *et al.*, *Proc. Natl. Acad. Sci. U.S.A.* **100**, 2065 (2003).
14. J. H. L. P. Sadowski *et al.*, *Cell Rep.* **14**, 1916 (2016).
15. Y. Frégnac, *Science* **358**, 470 (2017).

10.1126/science.aat1493